ChemSusChem

Research Article
doi.org/10.1002/cssc.202202213

Chemistry
Europe
European Chemical
Societies Publishing

www.chemsuschem.org

Self-Activation of Inorganic-Organic Hybrids Derived through Continuous Synthesis of Polyoxomolybdate and *para*-Phenylenediamine Enables Very High Lithium-Ion Storage Capacity

Mana Abdirahman Mohamed,[a] Stefanie Arnold,[b, c] Oliver Janka,[a] Antje Quade,[e] Volker Presser,*[b, c, d] and Guido Kickelbick*[a]

Inorganic-organic hybrid materials with redox-active components were prepared by an aqueous precipitation reaction of ammonium heptamolybdate (AHM) with *para*-phenylenediamine (PPD). A scalable and low-energy continuous wet chemical synthesis process, known as the microjet process, was used to prepare particles with large surface area in the submicrometer range with high purity and reproducibility on a large scale. Two different crystalline hybrid products were formed depending on the ratio of molybdate to organic ligand and pH. A ratio of *para*-phenylenediamine to ammonium heptamolybdate from 1:1 to 5:1 resulted in the compound $[C_6H_{10}N_2]_2[Mo_8O_{26}] \cdot 6\ H_2O$, while higher PPD ratios from 9:1 to 30:1 yielded a composition of $[C_6H_9N_2]_4[NH_4]_2[Mo_7O_{24}] \cdot 3\ H_2O$. The electrochemical behavior of the two products was tested in a battery cell environment. Only the second of the two hybrid materials showed an exceptionally high capacity of 1084 mAh g^{-1} at 100 mA g^{-1} after 150 cycles. The maximum capacity was reached after an induction phase, which can be explained by a combination of a conversion reaction with lithium to Li_2MoO_4 and an additional in situ polymerization of PPD. The final hybrid material is a promising material for lithium-ion battery (LIB) applications.

Introduction

The ever-growing demand for portable electronic devices and larger energy storage systems requires optimization and continuous expansion of lithium-ion battery (LIB) technology.

[a] M. A. Mohamed, Dr. O. Janka, Prof. Dr. G. Kickelbick
Inorganic Solid-State Chemistry, Saarland University
Campus C4 1, 66123 Saarbrücken (Germany)
E-mail: guido.kickelbick@uni-saarland.de
Homepage: https://www.uni-saarland.de/en/chair/kickelbick.html

[b] S. Arnold, Prof. Dr. V. Presser
INM—Leibniz Institute for New Materials
66123 Saarbrücken (Germany)
E-mail: volker.presser@leibniz-inm.de
Homepage: http://www.leibniz-inm.de/en/research/interface-materials/
energy-materials/

[c] S. Arnold, Prof. Dr. V. Presser
Department of Materials Science and Engineering, Saarland University
66123 Saarbrücken (Germany)

[d] Prof. Dr. V. Presser
Saarene—Saarland Center for Energy Materials and Sustainability
66123 Saarbrücken (Germany)
Homepage: http://saarene.de

[e] Dr. A. Quade
Leibniz Institute for Plasma Science and Technology
Felix-Hausdorff-Straße 2, 17489 Greifswald (Germany)
Homepage: https://www.inp-greifswald.de/en/

The success of this technology is based on its superior energy density, long cycle life, and reliable stability, explaining the dominance of LIB among present-day electrochemical energy storage devices. The most often used anode material in LIBs is graphite, which is limited to a delithiation capacity of 372 mAh g^{-1} (with a stoichiometry of LiC$_6$).[1] Therefore, other materials, such as mixed metal oxides e.g. $Li_4Ti_5O_{12}$ (LTO),[2] or nanoparticles of transition metal oxides, such as CoO, CuO, and Fe_2O_3, are currently under investigation for an improved battery performance.[3–5] One of the major problems with some new electrode materials is the significant volume change during lithiation and delithiation, which can lead to fractures in the electrode and often results in capacity fading.[6]

Inorganic-organic hybrid materials exhibiting redox activity are promising candidates for simultaneously solving several problems, for example, lower energy consumption during production or lower volume expansion during intercalation compared to traditional pure inorganic materials. Polyoxometalates (POMs), with their unique electrochemical redox properties and high stability with distinct oxidation and reduction states, are ideally suited as the inorganic component in such materials.[7] One of the most prominent examples is the phosphomolybdate anion, especially $[PMo_{12}O_{40}]^{3-}$ with a Keggin structure that shows fast and reversible electron transfer reactions without changing its molecular geometry.[7,8] Pure polyoxomolybdates $[Mo_7O_{24}]^{6-}$ and $[Mo_8O_{26}]^{4-}$ show redox activity and are readily available through acidifying an aqueous molybdate solution.[9] Particularly, the heptamolybdate anion $[Mo_7O_{24}]^{6-}$ is an exceptionally redox-active polycounterion showing metal-centered redox processes.[10–12] One strategy to increase capacity is to blend POMs with redox-active organic

ChemSusChem

Research Article
doi.org/10.1002/cssc.202202213

Chemistry Europe
European Chemical
Societies Publishing

molecules to yield inorganic-organic hybrid materials. *para*-Phenylenediamine (PPD) represents an excellent redox mediator through a two-electron oxidation-reduction reaction. Moreover, PPD can polymerize under electrochemical conditions.[13–16] Furthermore, the two nitrogen atoms provide a possible coordination site for Li$^+$ during the lithiation-delithiation process. Therefore, they can improve the Li mobility of hybrid materials made of this organic compound. An example of a redox-active inorganic-organic hybrid system is the combination of phosphomolybdate polyanion $[PMo_{12}O_{40}]^{3-}$ and a polyaniline matrix, which was applied as cathode materials for LIBs.[8] Also, POM-based metal–organic frameworks (POMOFs) materials,[17] a POM-incorporated metallapillararene metal–organic framework (MOF),[18] and metallacalixarene MOFs with different Keggin type polyoxometalates showed already promising electrochemical performance as LIB anode materials.[18] Porous POMOF anode materials revealed high chemical stability and reached a capacity of 710 mAh g^{-1} after 50 cycles with a specific current of 100 mA g^{-1}. The likewise promising capacity retention of 82% at a high rate of 800 mA g^{-1} after 500 cycles complement these findings.[19] A stable chiral three-dimensional POM-based MOF built by achiral 1,3-bis-(4-pyridyl)propane (BPP) and Zn-ε-Keggin showed an enhanced electrochemical activity as an anode of LIBs reaching a highly reversible capacity of 1004 mAh g^{-1} at 100 mAh g^{-1} after 100 cycles.[20] Finally, Zhang et al. presented a new redox-active poly-counterion doping concept that improves the capacity performance of conducting polymers.[11]

To further advance LIB technology, improved performance of electrode materials must be combined with the possibility of large-scale production processes. Our previous studies have shown that precipitation methods, usually carried out in batch processes, can be converted into a continuous process by using a so-called microjet reactor.[21,22] This opens up the possibility for large-scale and low-energy-consuming production of well-defined (nano)particles. In this process, two reactant solutions are fed under high pressure into a reaction chamber where rapid mixing takes place and the nucleation process is initiated. A gas jet then removes the product from the mixing chamber, and particle growth takes place on the way to the collection vessel. The separation of nucleation and growth allows good control of particle properties and has already been used in the production of silicon oxycarbides for LIB applications.[23–25] The main advantages of this process in the production of energy materials are its scalability, low energy consumption, and avoidance of additional additives.[26]

In this work, we present a systematic study of the formation of an inorganic-organic hybrid material precipitated from *para*-phenylenediamine (PPD) and ammonium heptamolybdate (AHM). PPD fulfills two roles here, firstly it can be protonated during the acid precipitation process and replaces the charge balancing ammonium ions, secondly it can support the electrochemical activity of the hybrid materials formed by its own redox activity. Hybrid materials with similar composition were known from literature as precursors for pyrolytic preparation of Mo_2C.[27] In contrast to previously published work in which the hybrid materials were thermally decomposed, we asked

ourselves whether the thermally untreated materials could already be used as potential electrode materials. It was important to find out whether the ratio between organic and inorganic components in the precipitation reaction also has an effect on the composition of the precipitated product and its electrochemical activity.

Results and Discussion

Precipitation reaction of inorganic-organic hybrid material

Inorganic-organic hybrid materials are formed by a precipitation reaction in an aqueous solution by mixing AHM as a molybdenum source with PPD under acidic conditions (Figure 1).

For the precipitation of the hybrid material, the organic molecules must have Lewis-basic functional groups that allow the formation of cations under acidic conditions and allow a full or partial exchange of the ammonium ions in the starting material. The resulting precipitate forms a salt between the molybdate anions and PPD cations.

Prior to the use of the microjet, various molar ratios between the organic compounds and the molybdenum source (1:1 to 30:1) were applied in initial batch reactions to investigate the correlation between the formation of inorganic-organic hybrid materials and the reactants used. These studies were transferred to the continuous production of the inorganic-organic hybrid materials with a microjet reactor, which allows the continuous formation of these precipitates.[21,22] Reactant
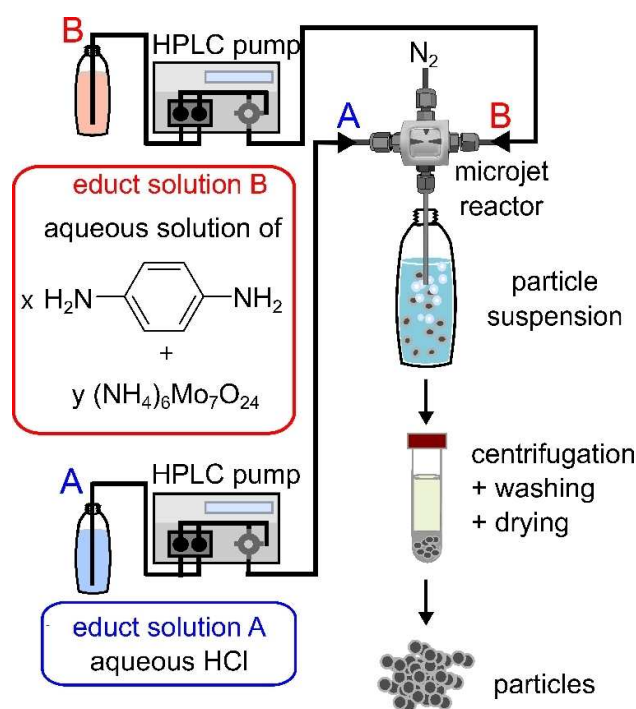

Figure 1. General reaction scheme for the production of the PPD/molybdate products.

ChemSusChem

Research Article
doi.org/10.1002/cssc.202202213

**Chemistry
Europe**
European Chemical
Societies Publishing

solutions 1 contained AHM and PPD in addition to a diluted solution of HCl (reactant solution 2, see experimental section).

Various analytical methods were used to characterize the product formed. For example, FTIR spectroscopy detected a broad band at 3550–3350 cm^{-1}, which can be assigned to the stretching vibration of the N–H group of PPD.[28] In addition, a broad band at 3600–3200 cm^{-1} indicates the presence of water.[29] The vibrations at 1650–1550 cm^{-1} are based on the bands of N–H deformation vibrations. In addition, there are C=C stretching vibrations at 1500–1480 cm^{-1}. Moreover, the typical bands of molybdate entities are found between 935 cm^{-1} and 810 cm^{-1} (Figure 2a). These observations confirm the incorporation of the organic and the inorganic components in the precipitates.[30–33] A comparison of the FTIR spectra of the
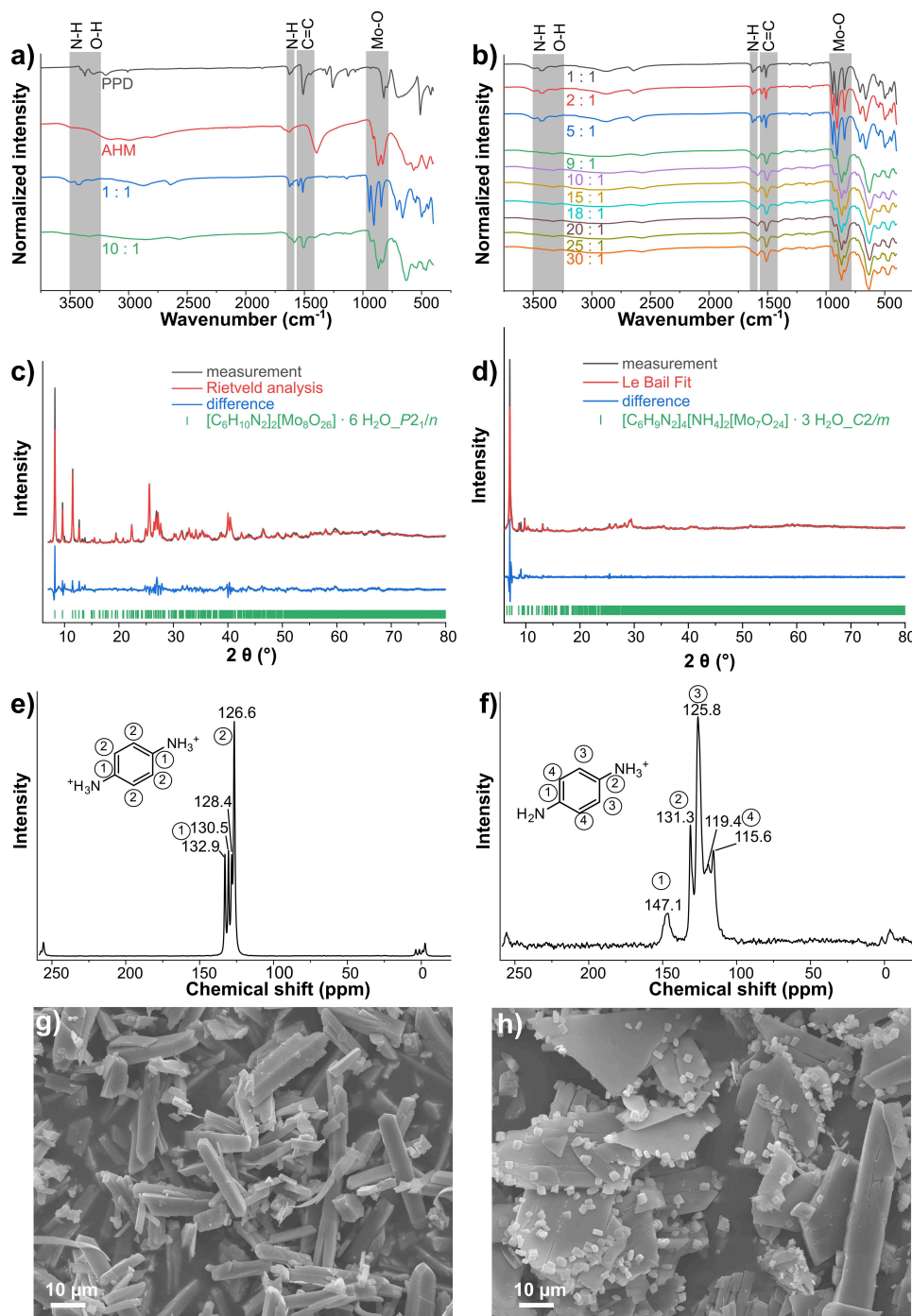

Figure 2. Material characterization: (a) FTIR spectra of PPD/molybdate precipitates in different ratios compared to their reactants. (b) FTIR spectra of PPD/molybdate in different ratios. (c,d): X-ray diffractograms of two different PPD/molybdate precipitates (ratios 10:1 and 1:1). (c) Rietveld refinement of PPD/molybdate (1:1). (d) Le Bail fit of PPD/molybdate (10:1). Differences in the intensities can be attributed to texture problems or preferred orientation. (e,f): ^{13}C CP-MAS NMR spectra. (g) Scanning electron micrograph of PPD/molybdate (1:1). (h) Scanning electron micrograph of PPD/molybdate (10:1).

PPD/molybdate precipitates revealed that the samples with the ratios 1:1, 2:1, and 5:1 containing low amounts of PPD differ from those with higher organic ligand content (Figure 2b).
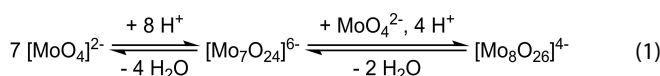
Elemental analyses for the precipitates (see Supporting Information, Table S1) reveal two regions with different compositions depending on the mixing ratio, indicating the formation of at least two different compounds. The samples with ratios of 1:1, 2:1, and 5:1 correspond to the composition $[C_6H_{10}N_2]_2[Mo_8O_{26}]\cdot 6\,H_2O$. In contrast, the samples with a mixing ratio from 9:1 to 30:1 indicate a composition in line with $[C_6H_9N_2]_4[NH_4]_2[Mo_7O_{24}]\cdot 3\,H_2O$.

Powder X-ray diffraction confirmed the existence of the literature known product $[C_6H_{10}N_2]_2[Mo_8O_{26}]\cdot 6\,H_2O$ in the precipitate of the PPD to AHM ratios 1:1 up to 5:1 (Figure S2a). No other phases corresponding to side products were observed in all those diffractograms. $[C_6H_{10}N_2]_2[Mo_8O_{26}]\cdot 6\,H_2O$ crystallizes in the monoclinic crystal system with the space group $P2_1/n$ and lattice parameters $a=834.31(9)$, $b=2145.8(3)$, $c=1027.6(1)$ pm, and $\beta=99.415(2)$.[34] The structure of the compound, which was previously characterized by single-crystal X-ray analysis, showed the existence of two octamolybdate anions, $[Mo_8O_{26}]^{4-}$, four double-protonated PPD cations, and twelve water molecules per unit cell. The octamolybdate clusters $[Mo_8O_{26}]^{4-}$ are surrounded by H_2PPD^{2+} cations with an open channel structure and octamolybdate clusters as guests (Figure S1).[34] Larger amounts of PPD (mixing ratio from 9:1 to 30:1) lead to different diffraction patterns (Figure S2a) and significantly different composition, based on the data from elemental analysis. Structural investigations on single crystals of this compound are extremely difficult since it crystallizes as very thin hexagonal platelets (Figure S3), which are very fragile and show a high degree of stacking faults. From the obtained dataset, a monoclinic structure with a space group C2/m and lattice parameters of $a=2029.9(1)$ pm, $b=1819.6(1)$ pm, $c=2521.2(1)$ pm, and $\beta=90.6(1)°$ and the presence of four $HPPD^+$ and one $[Mo_7O_{24}]^{6-}$ anion per formula unit can be deduced (Figure S4). The monoprotonated PPD cations can be unambiguously deduced when measuring the pH value of the supernatant from which the crystals were obtained. The measured pH was 4.4, therefore, when using the pK_a values from the literature ($pK_{a1}=2.67$, $pK_{a2}=6.2$),[35] only the first protonation can take place. For reasons of electroneutrality, two NH_4^+ cations must be present in the crystal structure. From the difference Fourier maps, the remaining electron density was attributed to these two ammonium cations and water molecules with the NH_4^+ cations being arbitrarily located. A total of 3 H_2O molecules could be derived, however, severe disorder of these is present. This results in a sum formula of $[C_6H_9N_2]_4[NH_4]_2[Mo_7O_{24}]\cdot 3\,H_2O$. Details on the structural determination can be found in the Supporting Information (Tables S2 and S3).

The information obtained from the structural analysis agrees well with combination of the previously discussed CHN (Table S1), X-ray data (Figure S2a), and TGA-FTIR data (thermogravimetric analysis coupled with Fourier-transform infrared spectroscopy; Figure S7).

The transition range 5:1 to 9:1 between the observed formation of the two compounds was studied in more detail. For this purpose, the mixing ratios 6:1, 7:1, and 8:1 were investigated. At the mixing ratio of 6:1, the formation of $[C_6H_{10}N_2]_2[Mo_8O_{26}]\cdot 6\,H_2O$ occurs, but there are also new reflections indicating the formation of a new component. At a mixing ratio of 7:1, the reflections of $[C_6H_9N_2]_4[NH_4]_2[Mo_7O_{24}]\cdot 3\,H_2O$ are observed, along with some new reflections that were also visible at 6:1. Finally, at a mixing ratio of 8:1, only $[C_6H_9N_2]_4[NH_4]_2[Mo_7O_{24}]\cdot 3\,H_2O$ appears to form (Figure S2b). Rietveld refinement based on the single-crystal data from the literature was performed for the PPD/molybdate precipitate with mixing ratios from 1:1 to 5:1 (Figure 2c). For mixing ratios of 9:1 to 30:1, Le Bail refinements were performed using the structural information obtained from the single crystal investigations (Figure 2d).

Since the reaction conditions (temperature, total volume, amount of hydrochloric acid) were kept constant and only the AHM to PPD ratio was varied, the synthesis of the inorganic-organic hybrid material seems to depend mainly on two parameters: (I) the content of organic components and thus (II) the pH of the solution. It is known that an acidic reaction leads to the condensation of ortho-molybdates enabling the formation of larger molybdate clusters [Eq. (1)].[9,34,36,37] An increasing PPD content results in an increase of the pH, thus removing protons from the system, and subsequently hampering the formation of the octa-molybdate cluster, underlining the observation of a hepta-molybdate cluster in the precipitate of the reactions containing a high PPD to molybdate ratio.

$$7\,[MoO_4]^{2-} \underset{-\,4\,H_2O}{\overset{+\,8\,H^+}{\rightleftharpoons}} [Mo_7O_{24}]^{6-} \underset{-\,2\,H_2O}{\overset{+\,MoO_4^{2-},\,4\,H^+}{\rightleftharpoons}} [Mo_8O_{26}]^{4-} \qquad (1)$$

^{13}C CP-MAS NMR spectra (cross polarization-magic angle spinning nuclear magnetic resonance spectra) of the PPD/molybdate (Figure 2e,f) confirm the presence of double protonated diamines in PPD/molybdate (1:1) (H_2PPD^{2+}) (Figure 2e) and mono-protonated diamines in PPD/molybdate (10:1) ($HPPD^+$) (Figure 2f). The presence of two different compounds forming in the respective precipitates is supported by scanning electron microscopy (SEM; Figure 2g,h). Variations of morphologies of the crystals were observed for different precipitates (Figure S3). Smaller amounts of PPD lead to anisotropic rod-shaped morphologies. In comparison, larger PPD amounts lead to sheet-like morphologies, which underpins the formation of different compositions depending on the AHM:PPD ratio obtained by CHN analysis. The temperature in the microjet synthesis influences the particle size. Thus, increasing temperature leads to smaller particle sizes (Figure S5).

Thermogravimetric analysis (TGA) provides valuable information on the synthesized inorganic-organic hybrid material (Figure S6). Pristine AHM shows three mass loss events up to 300 °C, based on the loss of water and ammonia.[38] According to the literature, after the decomposition of the precipitate, MoO_3 has formed, which sublimes and leads to the observed mass loss.[38] The sublimation of MoO_3 starting at 600 °C can be explained by its relatively high vapor pressure.[39–42] For the

ChemSusChem

Research Article
doi.org/10.1002/cssc.202202213

Chemistry
Europe
European Chemical
Societies Publishing

PPD/molybdate precipitates, two different trends of the TGA curves are visible. At low PPD concentration (exemplarily shown for the 1:1 ratio), the TGA curve show three mass losses, while at higher concentrations (10:1) only two mass losses were observed. For the 1:1 ratio, the first mass loss originates from the desorption of adsorbed surface water and the second from the loss of crystal water. The decompositions of the precipitates show similar thermal behavior to carbon-supported ammonium molybdate decomposition.[34] These conclusions are supported by TGA-FTIR measurements (Figure S7). According to the chemical composition $[C_6H_{10}N_2]_2[Mo_8O_{26}] \cdot 6\,H_2O$ the loss of six water molecules fits the value of the second mass loss. The third mass loss at around 700 °C shows the loss of CO and CO_2, leading to carbide phase formation. In contrast, the first mass loss observed at higher PPD concentrations results from the release of water and ammonia at around 192 °C, and the second mass loss is again the decomposition of the organic component, proven by the detection of CO and CO_2.

Electrochemical characterization of PPD/molybdate as LIB anode

The various synthesized hybrid materials were investigated for their suitability for energy storage systems. The materials were subjected to conventional LIB processing, namely, casting after compounding with carbon black conductive additive and polyvinylidene fluoride binder. Cyclic voltammetry was performed at different scan rates (0.1–10 mV s⁻¹) in the voltage range from 0.01 V to 3.00 V vs. Li⁺/Li to evaluate the underlying lithium-storage mechanism in the obtained electrodes (Figures 3a,b and S8). For both hybrid systems (PPD/molybdate (1:1) and PPD/molybdate (10:1)), one clear reduction/oxidation peak couple is found at 1.3 V and 1.5 V vs. Li⁺/Li, respectively. The transformation reaction, involving the formation of amorphous Li_2O and complete reduction of the molybdates, can be attributed to the obtained region when the lithiation potential decreases from 1.5 V to 0.05 V vs. Li⁺/Li.[43]

The pseudocapacitive feature can be further investigated by a kinetic analysis that includes an analysis of the rate-dependent current signal. The relationship between the current (i) and scan rate (v) is given by $i = av^b$, where a and b characterize the fitting parameters. Thereby obtained b-values of 0.5 correspond to an ideal diffusion-limited charge storage process typical for battery-like behavior. At the same time, a b-value of 1 indicates a perfect surface-limited charge storage process typical for electrosorption processes/capacitive processes.[44–46] The b-value analysis conducted on cyclic voltammetry is shown in Figure S9. The pronounced lithiation-delithiation peak of PPD/molybdate (1:1) shows a b-value of 0.82 and 0.79, respectively. The more pseudocapacitive regions at 0.62 V and 2.75 V vs. Li⁺/Li exhibit slightly enhanced b-values of 0.94 and 0.82 for delithiation, respectively. For the same regions in the lithiation curve, however, we obtain lower values of 0.71 and especially 0.56, which are closer to the values for the ideal diffusion-limited charge storage process. The b-value analysis of PPD/molybdate (10:1) provides for the pronounced lithiation-delithiation peak

of PPD/molybdate (10:1) a b-value of 0.63 and 0.74. The additional values obtained at 0.62 V and 2.75 V vs. Li⁺/Li characterize significantly more pseudocapacitive regions with much higher b-values of 0.91 and 0.93 for delithiation and 0.73 as 0.86 for lithiation, respectively.

To further investigate the electrochemical performance and associated conversion reaction of the different hybrid samples, galvanostatic charge and discharge experiments were performed. The obtained reduction and oxidation peaks from cyclic voltammetry are consistent with the galvanostatic discharge and charge curves (Figure 3c,d). No clear plateaus can be detected for the PPD/molybdate (1:1) sample, which cannot be assigned to associated (redox) reactions. In the sample with a higher insertion of PPD, there is no pronounced plateau in the first cycles, but after a while, there are two clear plateaus at 1.35 V and 0.8 V vs. Li⁺/Li. This indicates that different reactions occur during cycling, supported by continuously increased capacity observed during the first cycles. In general, an increase in capacity is attributed to pre-activation of the material.[47,48] However, this cannot explain the persistent increase during more than 120 cycles, which started with a delithiation capacity of 195 mAh g⁻¹ and reached a very high value of 1084 mAh g⁻¹ in the 150th cycle (Figure 3e). This 556% increase must be related to a change in the electrode material. This behavior can be confirmed by post-mortem analysis, which shows a complete degradation of the material and the formation of crystalline Li_2MoO_4, as shown by the powder X-ray diffraction pattern in Figure 4b.

It is difficult to separate the theoretical specific capacity of the two components and infer the hybrid materials, because the capacity is not simply the combination of the two components, but depends on many different factors, such as the particle size, the morphology, the homogeneous distribution of the different components and on the interaction of the different components. This is a principle that is often observed in hybrid materials.

Our data suggests a mechanism characterized initially by ion intercalation and a gradual transition to a process dominated by the transformation reaction. This can be confirmed in the plateaus in the later cycle curves. This trend is seen to a lesser extent in the PPD/molybdate (1:1) sample and very pronounced in the PPD/molybdate (10:1) sample. Moreover, the galvanostatic lithiation-delithiation curves show a potential drift during the electrochemical measurement of the battery cell. The plateau of the lithiation curve shifts toward higher capacity, while the plateau of the delithiation curve also shifts slightly in that direction. The reasons for these shifts may be a change in kinetics, undesirable side reactions, and a change in the reaction mechanism. During cycling, the slope of the discharge curves of the PPD/molybdate (10:1) sample also changed, i.e., flattened. This may be associated with a reduction in the grain size of the electrode material during cycling.[45] Although the charge storage process is Faradaic, the charge transfer and storage are kinetically much faster than conventional battery materials with significantly different redox peaks.[49,50] The hybrid PPD/molybdate (10:1) material clearly indicates that the structure obtained after the reaction

ChemSusChem

Research Article
doi.org/10.1002/cssc.202202213

**Chemistry
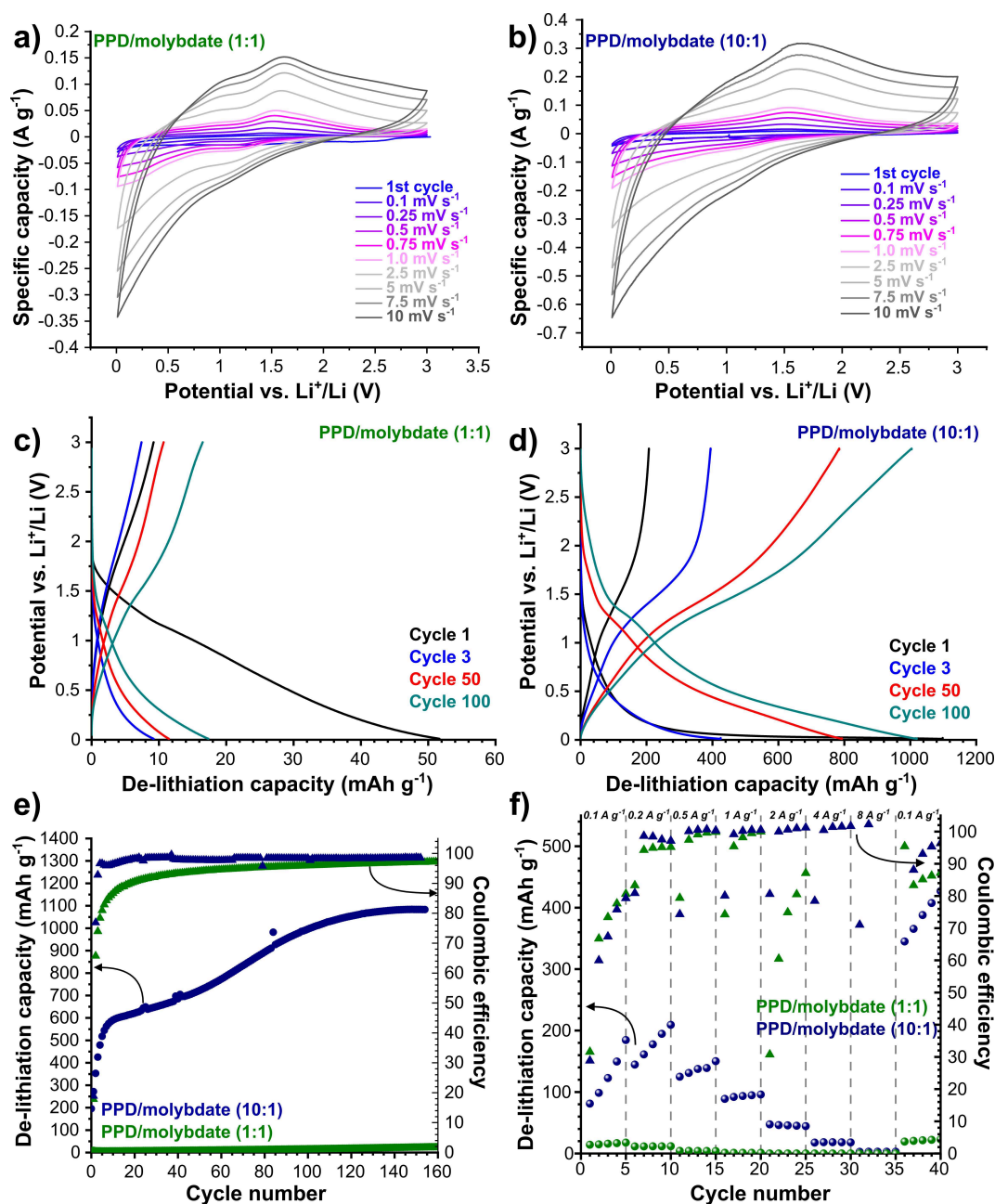Europe**
European Chemical
Societies Publishing

Figure 3. Electrochemical performance of PPD/molybdate hybrid materials: (a,b) Cyclic voltammograms at different scanning rates and potential range between 0.01 V and 3.00 V vs. Li$^+$/Li for (a) PPD/molybdate (1:1), and (b) PPD/molybdate (10:1). (c,d) Galvanostatic charge and discharge profiles at an applied specific current of 100 mA g^{-1} between 0.01 V and 3.00 V vs. Li$^+$/Li of (c) PPD/molybdate (1:1), and (d) PPD/molybdate (10:1). (e) Galvanostatic charge–discharge cycling performance showing the electrochemical stability with corresponding Coulombic efficiency values at a specific current of 100 mA g^{-1} for PPD/molybdate (1:1), PPD/molybdate (10:1). (f) Rate performance evaluated from galvanostatic charge-discharge cycling at different specific currents with corresponding Coulombic efficiencies for PPD/molybdate (1:1), PPD/molybdate (10:1).

in the microjet reactor is electrochemically very active and is further activated during cycling, making it a promising high capacity material for application in lithium-ion batteries. These observations can also be confirmed by the rate tests performed (Figure 3f), which show that the hybrid materials exhibit very unstable performances. This is especially true for the PPD/molybdate (10:1) sample, since pre-activation cannot occur and the capacities grow towards the fifth cycle of a rate. In contrast,

the PPD/molybdate (1:1) sample shows poor Coulombic efficiency above a specific current of 2 A g^{-1}.

Compared to other hybrid and composite MoO$_x$ systems (Table 1), the optimized inorganic-organic hybrid materials presented in this work provide very favorable electrochemical performance values (e.g., 1084 mAh g^{-1} after 150 cycles) for [C$_6$H$_9$N$_2$]$_4$[NH$_4$]$_2$[Mo$_7$O$_{24}$]·3 H$_2$O which can compete with results reported in "state-of-the-art" literature, with straightforward

ChemSusChem

Research Article
doi.org/10.1002/cssc.202202213

Chemistry Europe
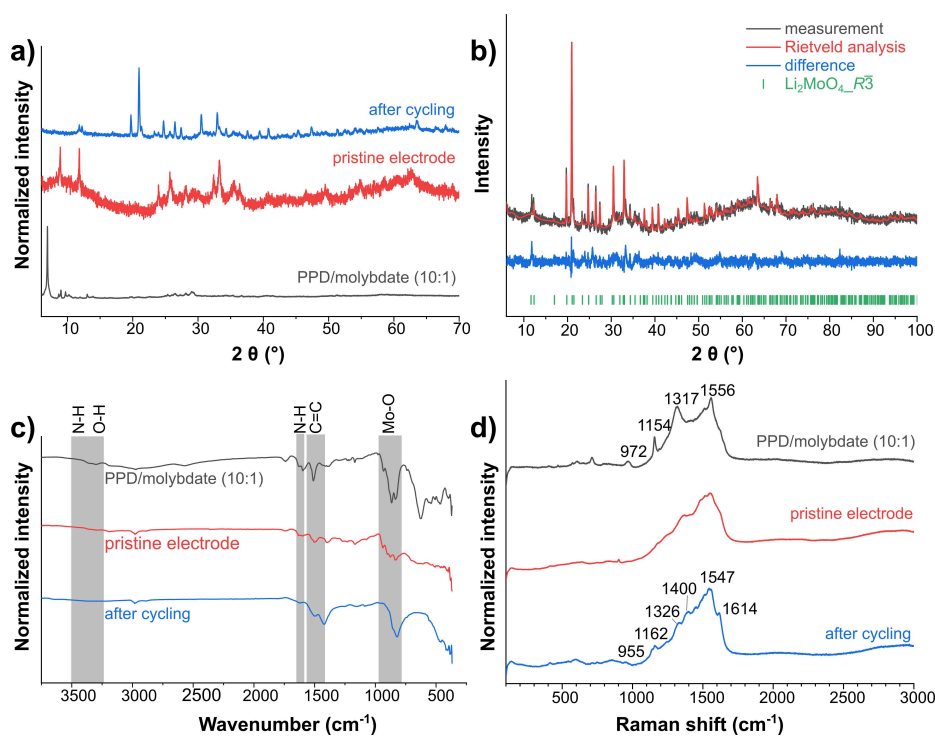European Chemical
Societies Publishing

Figure 4. (a) X-ray diffractograms of PPD/molybdate (10:1), pristine electrode, and the electrode after cycling. (b) Rietveld analysis of the cycled PPD/molybdate (10:1). (c) FTIR spectra of PPD/molybdate (10:1), pristine electrode material, and the electrode after cycling. (d) Raman spectra of PPD/molybdate (10:1), pristine electrode material, and the electrode after cycling.

Table 1. Summary of the different electrochemical performances and properties of various molybdenum oxide hybrid or composite materials. Data from literature sources that are not available are indicated as "n.a.". EC = ethylene carbonate; DEC = diethyl carbonate; EMC = ethyl methyl carbonate; DMC = dimethyl carbonates; PVdF = polyvinylidene fluoride; LiPF$_6$ = lithium hexafluorophosphate; CMC = carboxymethyl cellulose; CNT = carbon nanotubes; rGO = reduced graphene oxide.

Ref.	Material	Total electrode composition	Potential [V]	Electrolyte	Normalization	Capacity [mAh g^{-1}]	Cycles
Han et al.[51]	MoO$_3$/CNT	MoOx/CNTs: Super P, PVdF 8:1:1	0.01–3.0	1 M LiPF$_6$ in EC/DEC (1:1 by volume)	n.a.	500 at 0.1 A g^{-1}	90
Chen et al.[54]	Amorphous MoO$_x$ Thin Films	n.a.	0.01–3.0	1 M LiPF$_6$ in EC/EMC/DMC (1:1:1 by volume)	n.a.	845 at 90 µA cm^{-2}	100
Han et al.[55]	nanoporous graphene/molybdenum oxide	n.a.	0.01–3.0	1 M LiPF$_6$ in EC/DMC (1:1 by volume)	n.a.	710 at 1 A g^{-1}	150
Larson et al.[56]	Molybdenum oxide nanoporous asymmetric membranes	52% MoO$_2$ 48% C	0.01-3.0	1 M LiPF$_6$ in EC/DMC/DEC (1:1:1 by volume)	n.a.	480 at 0.12 A g^{-1}	150
Naresh et al.[57]	MoO$_3$ /rGO	active material: Super P: PVdF 8:1:1	0.1–2.5	1 M LiPF$_6$ in EC/DMC (1:1 by volume)	n.a.	568 at 0.5 A g^{-1}	100
Xin et al.[53]	Mo$_2$C@C core-shell nanocrystals	active material: acetylene black: sodium alginate 7:2:1	0.01–3.0	1 M LiPF$_6$ in EC/EMC/DMC (1:1:1 by volume)	n.a.	1089 at 0.1 A g^{-1}	100
Yang et al.[52]	MoO$_2$–Mo$_2$C–C	MoO$_2$–Mo$_2$C–C: acetylene black: CMC 7:2:1	0.01–3.0	1 M LiPF$_6$ in EC/DC (1:1 by volume)	n.a.	1188 at 0.1 A g^{-1}	250
Gao et al.[58]	MoO$_2$/C hybrid	MoO$_2$/C hybrid: acetylene: PVdF 8:1:1	0.01–3.0	1 M LiPF$_6$ in EC/DEC (1:1 by volume)	n.a.	700 at 0.2 A g^{-1}	100
Our work	[C$_6$H$_9$N$_2$]$_4$[NH$_4$]$_2$[Mo$_7$O$_{24}$]·3 H$_2$O hybrid	Mo-hybrid: conductive carbon additive: PVdF 8:1:1	0.01–3.0	1 M LiPF$_6$ in EC/DMC (1:1 by volume)	Total hybrid	1084 at 0.1 A g^{-1}	150

processing. For example, the optimized MoO$_2$ and MoO$_3$/CNTs nanocomposites in the work of Han et al.[51] provide less than half of our capacity (500 mAh g^{-1}) with very low cycling stability (90 cycles). The MoO$_2$–Mo$_2$C–C microspheres in the work of Yang et al.[52] were based on a one-step annealing approach and provided an excellent reversible capacity of 1188 mAh g^{-1}

after 250 cycles at a specific current of 100 mA g^{-1}. The electrochemical behavior is very similar to our hybrid material even with the persistent increase in capacity, which is likely related to a change in the material and/or reaction mechanism. While slightly higher delithiation capacity is obtained after 250 cycles compared to our system, the capacities are very similar

ChemSusChem

Research Article
doi.org/10.1002/cssc.202202213

Chemistry
Europe
European Chemical
Societies Publishing

after 150 cycles when comparing the two systems (~ 1000 mAh g^{-1}). The coupled Mo$_2$C@C core-shell nanocrystals on 3D graphene fabricated in the work of Xin et al.[53] also show very comparable capacity values (reversible capacity of 1090 mAh g^{-1} after 100 cycles at 0.1 A g^{-1}).

After continuous microjet reactor synthesis, the materials obtained can directly achieve high electrochemical performance without additional thermal or chemical processing. By fine-tuning the synthesis conditions, a characteristic electrochemical behavior similar to that described in the literature for molybdenum oxides could be achieved. The possibility to further modify these components makes this type of inorganic-organic hybrid synthesis very promising for electrochemical storage.

Material characterization of PPD/molybdate LIB anodes

To explain the unexpected improvement in electrochemical performance of PPD/molybdate (10:1) during cycling, the original electrode and the post-cycling electrode were characterized by powder X-ray diffraction, FTIR spectroscopy, and Raman spectroscopy (Figure 4a–d). These measurements were compared with the as-synthesized PPD/molybdate (10:1). For this purpose, the electrodes were prepared after cycling by stopping the cells in the delithiated state after 100 cycles, and the obtained electrode was rinsed with DMC to remove the residual salt. The X-ray diffractograms (Figure 4a) show a clear change comparing the PPD/molybdate and the electrode. The diffraction pattern of the electrode seems to shift and the reflections broaden considerably, as would be expected if a reduction is associated with a decrease in crystallite size (see above). The crystallite size of PPD/molybdate (10:1) is 48(1) nm and decreases to 40(10) nm (average over eight reflections) after electrode preparation. After cycling, the X-ray diffractograms change significantly, confirming the formation of lithium molybdate (Li$_2$MoO$_4$; Figure 4b), which crystallizes in the trigonal crystal system with space group $R\bar{3}$ ($a = 1433.0(2)$ pm, $c = 958.4(2)$ pm).[59]

In the FTIR spectra (Figure 4c), the observed bands in the as-prepared electrode are still at the same positions, indicating that the same structure must be present. However, the broad water band in the range 3600–3200 cm^{-1} has disappeared.[29] This indicates that solvent exchange occurred during the electrode preparation. The FTIR spectrum of the cycled sample shows that the N–H bands at 1650–1550 cm^{-1} are no longer present. One possible reason for this is the deprotonation of the amine groups. This would make the nitrogen atom a possible coordination site for Li$^+$ during the lithiation-delithiation process. It is possible that PPD is involved in a redox reaction. In this case, p-benzoquinone diimine may be formed by a two-electron redox reaction. PPD can also be electrochemically polymerized in situ.[13–16] The splitting of the C=C band in the cycled sample can be assigned to C=C and C=N vibrations. This is consistent with the work on polymerized PPD found in the literature.[16,60,61]

Comparison of the different Raman spectra (Figure 4d) shows a clear change in the PPD/molybdate (10:1) and the cycled sample, indicating a polymerization. In PPD/molybdate (10:1), a band at 1556 cm^{-1} is observed, assigned to C=C vibrations. After cycling, the band shifts to 1547 cm^{-1}, and a new band appears at the shoulder at 1614 cm^{-1} corresponding to C=C and C=N vibrations. Other additional peaks at 1511 cm^{-1}, 1400 cm^{-1}, 1326 cm^{-1}, and 1162 cm^{-1} correspond to C–C, C–N, C–N$^+$, and C–H vibrations of the quinoid ring, respectively. The equivalent bands of the C–H and C–N vibrations are shifted to 1317 cm^{-1} and 1154 cm^{-1} in the PPD/molybdate (10:1) sample.[16,61] The Mo–O vibrations are visible at 972 cm^{-1} in the PPD/molybdate (10:1) sample, and after cycling the band shifts to 955 cm^{-1}. That highlights the observed change of the molybdate unit. The band at 972 cm^{-1} is assigned to Mo$_7$O$_{24}$$^{6-}$ units, while the band at 955 cm^{-1} corresponds to MoO$_4$$^{2-}$ units.[62]

X-ray photoelectron spectroscopy (XPS) measurements were performed to obtain information on the oxidation states of the Mo-species and the oxygen-bonding states. The Mo3d peaks were fitted with three components (Figure 5). The Mo^{6+} component has the highest binding energy with a binding energy of 232.6 eV. The signal caused by a reduced Mo^{m+} (presumably Mo^{5+}) species was fitted with a constant binding energy distance of -1.3 eV to Mo^{6+}, while Mo^{n+} (presumably Mo^{4+}) was fitted with a constant binding energy distance of -3 eV with respect to Mo^{6+}.[63]

The samples PPD/molybdate (1:1) (Figure 5a) and PPD/molybdate (10:1) (Figure 5b) were compared with the pristine electrode and the electrode after cycling to obtain further information about the redox processes taking place. Due to the high surface sensitivity of XPS spectroscopy, the information depth is about 10 nm. Therefore, only qualitative information is obtained. The precipitates PPD/molybdate (1:1) and PPD/molybdate (10:1) show the presence of Mo^{6+} (Figure 5a,b). In the pristine electrode of both samples, molybdenum species with lower oxidation numbers appear (Figure 5c,d). This indicates that the molybdenum has already been reduced during the electrode preparation step. After cycling, the content of Mo-species with a lower oxidation number increases in both samples. In addition, small contributions of even further reduced Mo^{4+} appear (Figure 5e,f). Thus, further reduction of the molybdenum species is observed, which can be attributed to electrochemical processes in the cell. A similar trend occurs for both samples PPD/molybdate (1:1) and PPD/molybdate (10:1), compared to their electrodes and the electrodes after cycling. These investigations show that both components the molybdenum species as well as the organic species contribute to the redox process.

The O1s peaks were fitted with four signals (Figure 6). The signal at 530.6 eV was used for calibration, which is due to the O–Mo^{6+} interaction. The O–Mo^{5+} contribution was observed at a binding energy of 531.2 eV. The binding energies assigned to O=C and O–Mo^{4+} bonds overlap at 532.0 eV, and the contribution originating from the O–C bond has a binding energy of 533.3 eV.[63] These binding energies agree well with the literature values. They can be explained by the higher electron
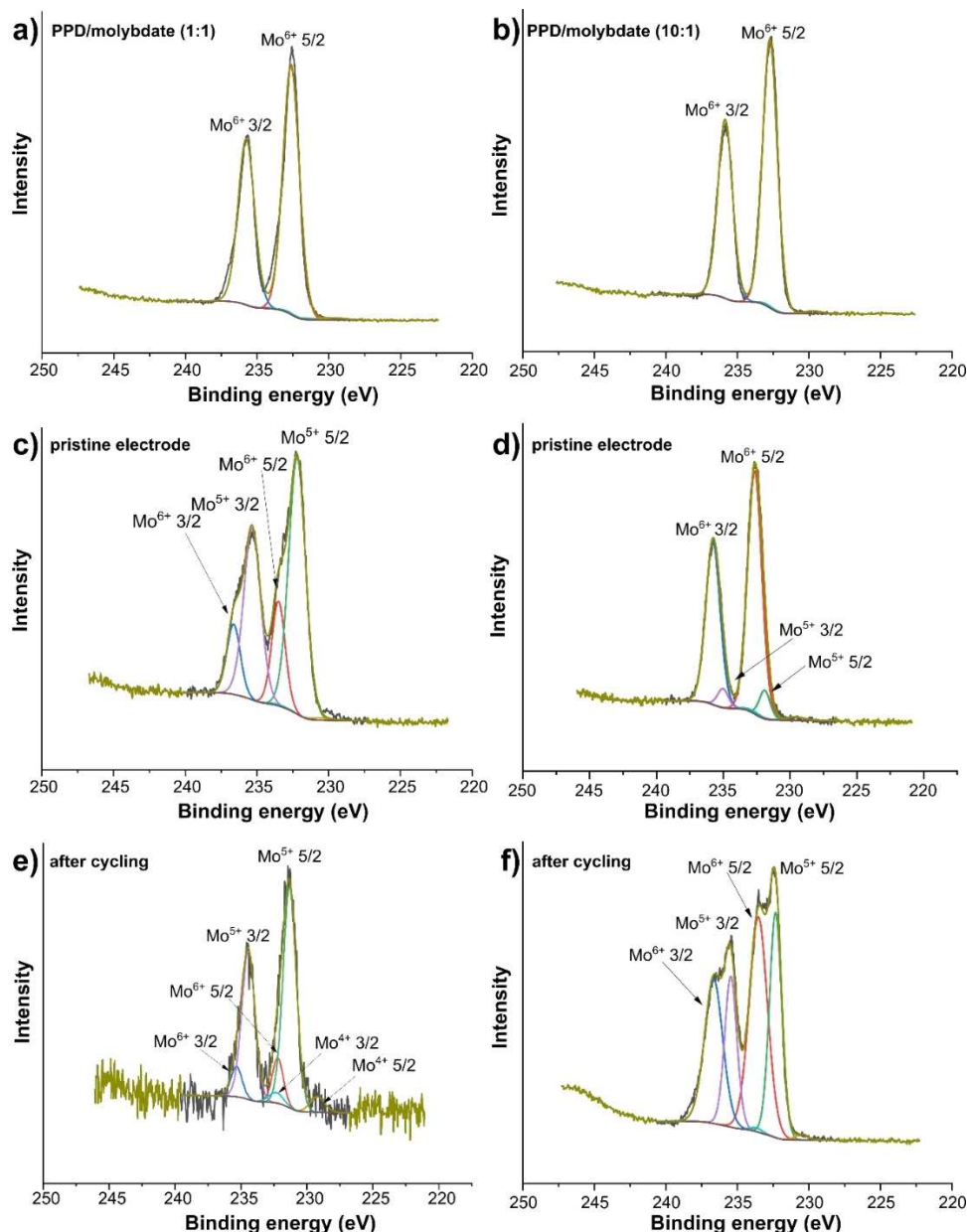
ChemSusChem

Research Article
doi.org/10.1002/cssc.202202213

Chemistry
Europe
European Chemical
Societies Publishing

Figure 5. Fitted XPS Mo3d spectra: (a) PPD/molybdate (1:1); (b) PPD/molybdate (10:1); (c) pristine electrode PPD/molybdate (1:1); (d) pristine electrode of PPD/molybdate (10:1); (e) electrode after cycling of PPD/molybdate (1:1); (f) electrode after cycling of PPD/molybdate (10:1).

density of the more electronegative oxygen when the metal atom is more oxidized, leading to a decrease in binding energy.[64] PPD/molybdate (1:1) (Figure 6a) and PPD/molybdate (10:1) (Figure 6b) have mainly O—Mo^{6+} bonds. In the pristine electrodes (Figure 6c,d) the proportion of O—Mo^{5+} increases, which correlates with the results of the Mo3d peaks. The observed O=C and C—O bonds may originate from the conductive additive (carbon black) used for the electrode preparation.

The cycled electrode of PPD/molybdate (1:1) (Figure 6e) exhibits O—Mo^{4+} and C—O bonds. The O1s peak of the cycled electrode of PPD/molybdate (10:1) (Figure 6f) is broader. It shows less O—Mo^{6+} and more O=C and C—O bonds, which is

due to the formation of lithium carbonate during the cycling process through the formation of a solid electrolyte interphase (SEI).[65] The original electrode of PPD/molybdate (1:1) contains the highest amount of O—Mo^{5+}, which correlates with the Mo bonds in Mo3d spectra. The amounts of O=C and O—C are comparable to those of other samples.

During electrode preparation, a change in the material is observed, as explained earlier. This change can be attributed to a chemical reaction of the material when treated with DMSO. The analyses (Figure S10) show that this leads to solvent exchange and a redox reaction. In the redox reaction induced this way, the PPD is partially oxidized and the DMSO and the
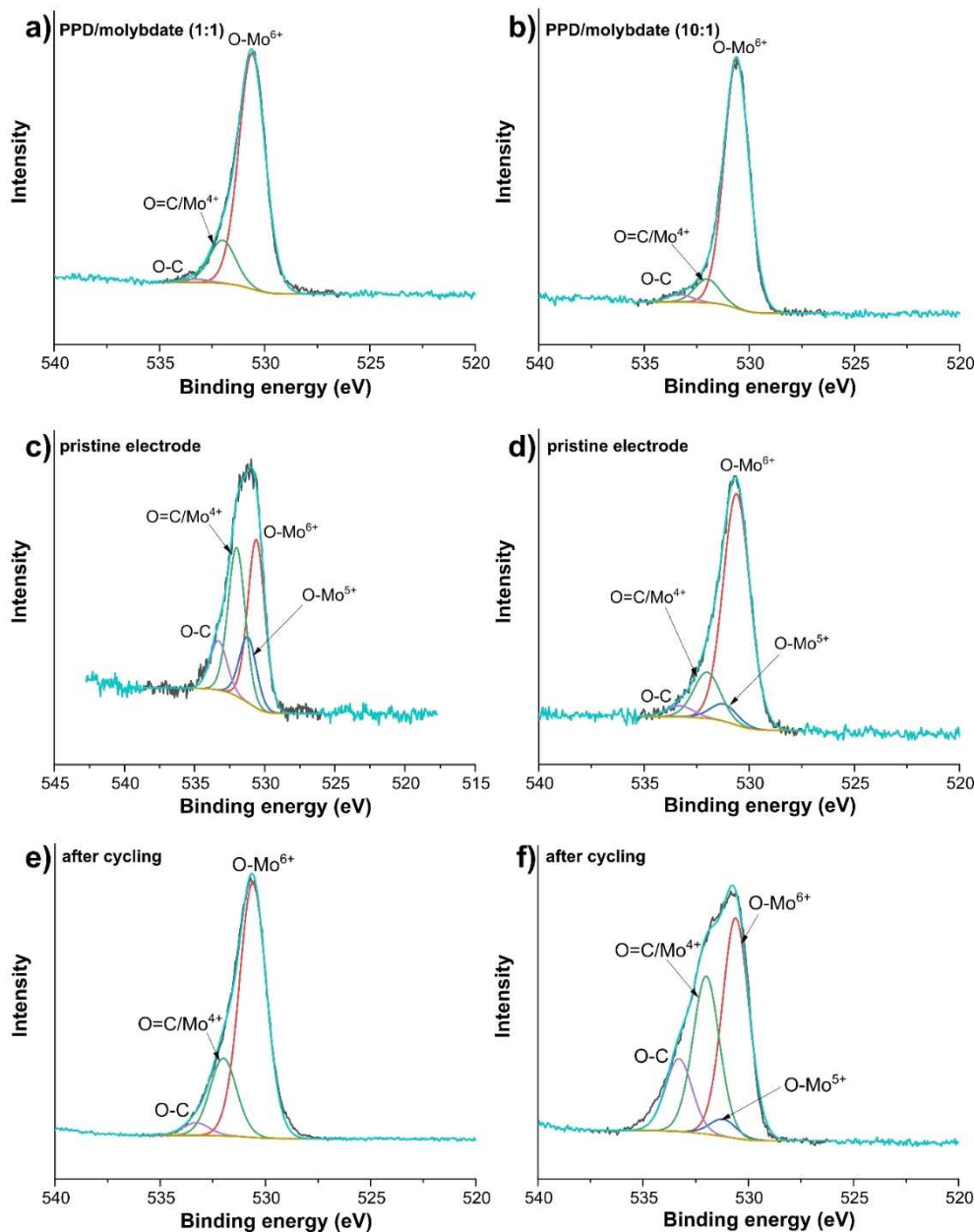
ChemSusChem

Research Article
doi.org/10.1002/cssc.202202213

**Chemistry
Europe**

European Chemical
Societies Publishing

Figure 6. Fitted XPS O1s spectra: (a) PPD/molybdate (1:1); (b) PPD/molybdate (10:1); (c) pristine electrode PPD/molybdate (1:1); (d) pristine electrode of PPD/molybdate (10:1); (e) electrode after cycling of PPD/molybdate (1:1); (f) electrode after cycling of PPD/molybdate (10:1).

molybdenum are partially reduced. This shows that the material is very redox-active.

Post-mortem analyses of the product were difficult due to the limited amount of material and the high content of various components. Therefore, we decided to carry out a model study applying a chemical lithiation instead of an electrochemically driven process. In this way, we obtained evidence for the description of electrochemical lithiation. PPD/molybdate treated with DMSO was subsequently chemically lithiated with *n*-butyllithium (*n*-BuLi) to produce a sample as close as possible to electrochemical lithiation (Figure 7). The product was then characterized by powder X-ray diffraction, FTIR spectroscopy and ^{13}C CP-MAS NMR spectroscopy. It can be concluded that a

redox-induced polymerization of the PPD takes place, resulting in a redox-active, positively charged poly(*p*-phenylenediamine) (Scheme 1). Composites of such polymers with metal species have proven to be highly conductive.[61]

Comparison of the X-ray diffraction patterns of DMSO-treated and chemically lithiated PPD/molybdate (10:1) after cycling, and PPD/molybdate (1:1) after cycling (Figure 7a) reveals the formation of the same phase. Using the structural data of trigonal Li_2MoO_4[59] the Rietveld analysis (Figure 7b) shows good agreement.

After chemical lithiation or electrochemical cycling, the molybdate component of the inorganic-organic hybrid material converts to Li_2MoO_4. This indicates that the electrochemical
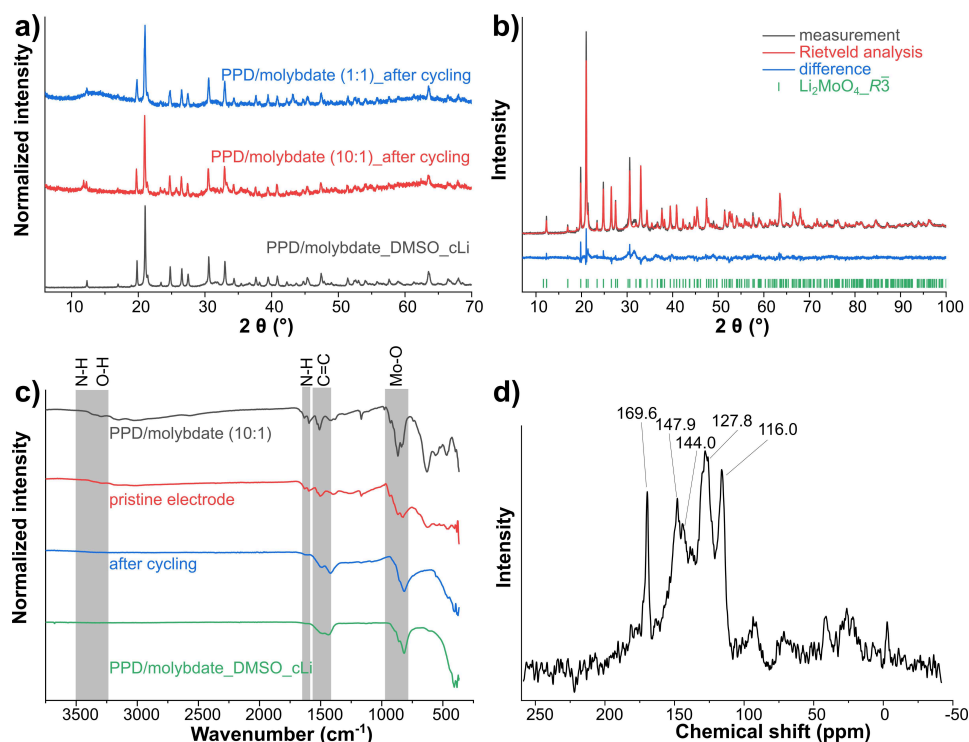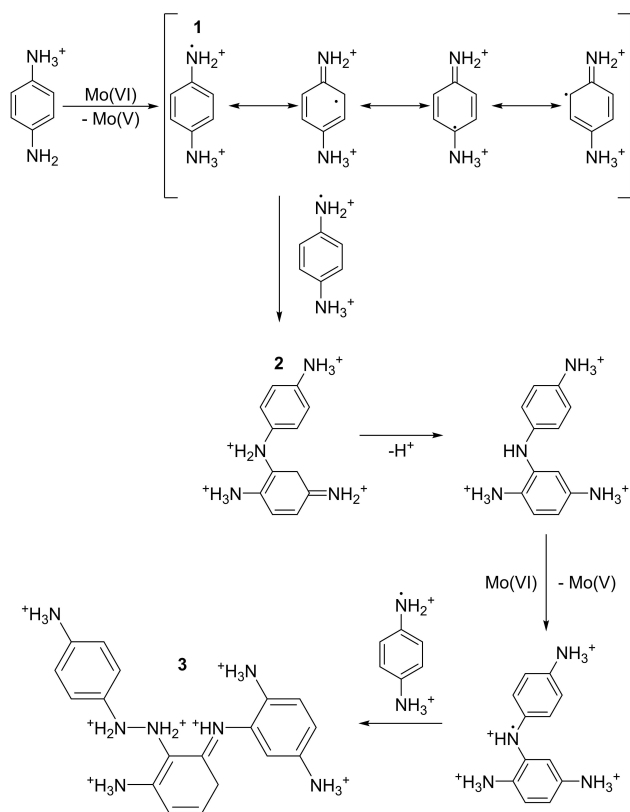
Figure 7. Results of chemical lithiation: (a) PXRD pattern of DMSO-treated and chemically lithiated PPD/molybdate, PPD/molybdate (10:1) after cycling and PPD/molybdate (1:1) after cycling. (b) Rietveld analysis of DMSO-treated and chemically lithiated PPD/molybdate. (c) FTIR spectra of PPD/molybdate (10:1), pristine electrode, after cycling and chemically lithiated PPD/molybdate_DMSO. (d) ^{13}C CP-MAS NMR spectrum of DMSO-treated and chemically lithiated PPD/molybdate.

cycling is reproducible by chemical lithiation with *n*-BuLi. It can be concluded that the molybdenum species contribute to the electrochemical activity, but the organic component seems to play a significant factor. Subsequently, the organic component was investigated in more detail by FTIR spectroscopy (Figure 7c) and ^{13}C CP-MAS NMR spectroscopy (Figure 7d). The FTIR spectra reveal that the bands of the DMSO-treated and chemically lithiated PPD/molybdate (10:1) and the PPD/molybdate (10:1) (Figure 7c) remain at the same position after cycling, indicating that the same organic species was formed. In the DMSO-treated PPD/molybdate (10:1) anode material used, a partial reduction of DMSO to DMS as well as Mo(VI) to Mo(V) takes place, which leads to partial oxidation of PPD to the corresponding benzoquinone diimine. The oxidative polymerization is activated during the electrochemical cycling. The ^{13}C CP-MAS NMR spectrum of DMSO-treated and chemically lithiated PPD/molybdate (Figure 7d) reveals the formation of a PPD trimer. The PPD dimer forms by recombination of the PPD cation radicals (Scheme 1). An N coupling of the PPD cation radical ([HPPD]$^{\bullet 2+}$) (**1**) is dominant upon dimerization. After dimerization, a new coupling with [HPPD]$^{\bullet 2+}$ and PPD dimer (**2**) occurs to form a PPD trimers (**3**). The peak at 169.6 ppm belongs to the carbon cation double-bonded to nitrogen (C=NH$^+$).[61]

Conclusions

In this work, a sustainable, continuous approach for the preparation of inorganic-organic hybrid materials with remarkable electrochemical properties using a microjet reactor is presented. Two inorganic-organic hybrid materials were synthesized from aqueous solutions of PPD and AHM at room temperature. The inorganic-organic hybrid material precipitated at low PPD:AHM ratios has the composition $[C_6H_{10}N_2]_2[Mo_8O_{26}] \cdot 6\,H_2O$, while the one at high PPD:AHM ratios contains a heptamolybdate anion and exhibits the composition $[C_6H_9N_2]_4[NH_4]_2[Mo_7O_{24}] \cdot 3\,H_2O$. The electrochemical measurements of PPD/molybdate (10:1) showed that an optimized electrode material could be produced by simply adjusting the synthesis parameters. Without further treatment, this material shows exceptional delithiation capacities through conversion reactions up to 1084 mAh g^{-1}. For reaching this high capacity the material requires an induction phase, which can be explained by several conversion reactions in the material during the redox processes. Both, the formation of Li$_2$MoO$_4$ and the polymerization of the PPD could be detected. The combination of inorganic and organic redox-active species in a hybrid material opens a large playground for the adjustment of specific properties. Moreover, the microjet approach represents a sustainable, energy-saving production method for such LIB materials.

ChemSusChem

Research Article
doi.org/10.1002/cssc.202202213

Chemistry Europe
European Chemical
Societies Publishing

Scheme 1. Proposed polymerization mechanism of PPD. Reproduced and modified from reference [61] with permission from John Wiley and Sons.

Experimental Section

Materials

Ammonium heptamolybdate tetrahydrate (AHM; $\geq 99\%$) was obtained from Carl Roth. *Para*-phenylenediamine (PPD; 97%) and *n*-Butyllithium (*n*-BuLi; 2.5 M in hexane, packaged under nitrogen in resealable AcroSeal bottles) were purchased from Alfa Aesar. The concentration of *n*-butyllithium was determined by titration to 2.27 M. The hydrochloric acid (HCl; 37%) was obtained from Bernd Kraft GmbH. Ethanol (99% denatured with 1% PE) and 2-propanol (97%) were received from BCD Chemie GmbH. Dimethyl sulfoxide (DMSO; 99%) was supplied from Fisher Scientific GmbH. Conductive carbon additive (Type C65) was purchased from IMERYS Graphite&Carbon, polyvinylidene fluoride (PVdF, 99.5%), dimethyl sulfoxide (DMSO, anhydrous, $\geq 99.9\%$), and lithium hexafluorophosphate (LiPF$_6$) (LP30; 1 M in an ethylene carbonate (EC) and dimethyl carbonate (DMC) mixture in the ratio EC:DMC (1:1 by volume) as electrolyte from Sigma Aldrich. All chemicals were used without further purification. VWR International GmbH provided *n*-hexane (> 97%). It was dried in a solvent purifying system SPS 5 (MBraun).

Synthesis

Beaker synthesis of precipitates

The general procedure for the precipitation formation was that AHM was dissolved in water (500 mL). The amine (these were added in different ratios; Table S4) was then dissolved in water (500 mL) and the two solutions were mixed, then dilute HCl

solution (1 L) was added, which led to the formation of a precipitate. Finally, the precipitates obtained from beaker synthesis were isolated by centrifugation (8000 rpm, 15 min). The products were washed with ethanol and dried at 80 °C.

Microjet synthesis

A diluted solution of HCl (solution A) and a mixture of AHM and the amines in water (solution B; Table S5) were used. AHM and the required amount of PPD were each dissolved in water (500 mL) to obtain solution B. For the microjet experiments, 1 L of each solution was used. Two high-performance liquid chromatography (HPLC) pumps (LaPrep P110 preparative HPLC pump, VWR) were used to transport the solutions with a flow rate of 250 mL min^{-1}. The reaction took place in the microjet reactor, where the solutions were forced through a nozzle with a diameter of 300 micrometers with high pressure into a reaction chamber. Nitrogen gas was used to remove the here-formed particles.[21] After the syntheses in the microjet reactor, the particles were isolated by centrifugation (8000 rpm, 15 min). The products were washed with ethanol and dried at 80 °C.

Chemical lithiation

For the chemical lithiation, PPD/molybdate (10:1)_DMSO (0.5 g) was first added to hexane (20 mL) under an argon atmosphere. To this was added 74 equivalents of *n*-butyllithium (2.27 M in *n*-hexane) with stirring. The reaction was stirred at 80 °C for 6 h. The reaction was terminated by the addition of 2-propanol to quench the remaining *n*-butyllithium. The product was separated by filtration. Finally, the product was washed with 2-propanol and dried at 80 °C.

Structural and chemical characterization

Fourier-transform infrared spectroscopy (FTIR) measurements of dried samples were recorded in attenuated total reflectance (ATR) mode using a Bruker Vertex 70 spectrometer. Each spectrum was performed in the wavenumber range 370–4500 cm^{-1} and by averaging 16 scans with a spectral resolution of 4 cm^{-1}. Thermogravimetric Analyses (TGA) were performed on a Netzsch TG F1 Iris under a constant flow of N$_2$ (40 mL min^{-1}) with a heating rate of 20 °C min^{-1} to a maximum of 900 °C. During the measurements, the samples were placed in an open alumina crucible. The TG-FTIR measurements were performed under the same conditions. The elemental analyses were conducted on an Elementar Vario Micro cube.

Powder X-ray diffraction (XRD) patterns of the pulverized samples were recorded at room temperature on a D8-A25-Advance diffractometer (Bruker) in Bragg-Brentano θ–θ geometry (goniometer radius 280 mm) with Cu$_{K\alpha}$-radiation ($\lambda = 154.0596$ pm). A 12 µm Ni foil working as K$_\beta$ filter and a variable divergence slit were mounted at the primary beam side. An LYNXEYE detector with 192 channels was used at the secondary beam side. Experiments were carried out in a 2θ range of 6° to 130° with a step size of 0.013° and a total scan time of 1 or 4 h. The recorded data was evaluated using the Bruker TOPAS 5.1 software, with the observed reflections being treated via single-line fits.[66]

The single-crystal data set was collected using a Bruker D8 Venture diffractometer with a microfocus sealed tube and a Photon II detector. Monochromated Cu$_{K\alpha}$ radiation ($\lambda = 1.54178$ Å) was used. Data was collected at 133(2) K and corrected for absorption effects using the multi-scan method. The structure was solved by direct methods using SHELXT[67] and was refined by full matrix least

ChemSusChem

Research Article
doi.org/10.1002/cssc.202202213

**Chemistry
Europe**
European Chemical
Societies Publishing

squares calculations on F^2 (SHELXL2018[68]) in the graphical user interface Shelxle.[69] Details on the single-crystal X-ray diffraction experiments is given in the Supporting Information. Deposition Number 2226468 contains the supplementary crystallographic data for this paper. These data are provided free of charge by the joint Cambridge Crystallographic Data Centre and Fachinformationszentrum Karlsruhe Access Structures service.

SEM images were recorded using a JEOL JSM-7000 F microscope with a working distance of 10 mm and operating at 20 kV. For the sample preparation, a small amount was placed on a specimen stub covered with a carbon adhesive foil, followed by the deposition of a gold layer.

Solid-state CP-MAS NMR spectra were recorded using a Bruker AV400WB spectrometer. A resonance frequency of 100.65 MHz for ^{13}C NMR spectra was used. The spinning frequency for the MAS experiments was 13 kHz. X-ray photoelectron spectroscopy (XPS) was performed with an Axis Supra (Kratos Analytical) spectrometer. Wide and elemental scans were acquired employing $Al_{K\alpha}$ radiation with 150 W power with a pass energy of 160 eV and 80 eV, respectively, while for high-resolution measurements, 225 W with 10 eV were used. The data processing was done with CasaXPS (Casa Software, version 2.3.15).

Raman spectra were recorded with a Renishaw inVia Raman Microscope equipped with a neodymium-doped yttrium aluminum garnet laser with an excitation wavelength of 532 nm and a laser power of approximately 0.05 mW at the surface of the sample, a $2400\,mm^{-1}$ grating, and a $50\times$objective lens with a numeric aperture of 0.75. Five different spots from each sample were recorded with five accumulations and 30 s acquisition time. All spectra were normalized to 100%.

Electrochemical characterization

Electrode materials and preparation

The hybrid material working electrodes were prepared by mixing 80 mass% $[C_6H_{10}N_2]_2[Mo_8O_{26}]\cdot 6\,H_2O$ or the $[C_6H_9N_2]_4[NH_4]_2[Mo_7O_{24}]\cdot 3\,H_2O$ powders, respectively, with 10 mass% conductive carbon additive (Type C65, IMERYS Graphite&Carbon) and 10 mass% polyvinylidene fluoride (PVdF, Sigma Aldrich), dissolved in dimethyl sulfoxide (DMSO, anhydrous, Sigma Aldrich), in a SpeedMixer DAC 150 SP from Hauschild. First, the active material and the conductive carbon were combined in a mortar and ground carefully. The dry powder mix was then dry-mixed for 5 min at 1000 rpm. Drop by drop, DMSO solvent was added to the mixture until the slurry reached the desired viscosity. This paste was again mixed at 1500 rpm for 5 min, following 2500 rpm for 5 min. Finally, the PVdF binder solution (10 mass% PVdF in DMSO) was added, and the viscous electrode past kept mixing for 10 min at 800 rpm. To obtain a homogenous electrode slurry, the suspension was agitated for 12 h using a magnetic stirrer. The obtained slurries were doctor-blade cast on copper foil with a wet thickness of 200 μm. The electrodes were initially dried at ambient conditions overnight. Then, a further vacuum drying step at 110 °C for 12 h was conducted to remove the remaining solvent. Dry-pressing in a rolling machine ((HR01 hot rolling machine, MTI) was used to regulate the electrode packing density. After that, utilizing press-punch (EL-CELL), 10 mm diameter discs were punched from the coating and used as the working electrode (WE). The resulting electrode thickness of the dried electrodes was 100 ± 10 μm with a material loading of $3.0\pm0.5\,mg\,cm^{-2}$.

Cell preparation and electrochemical characterization

For electrochemical testing in an organic electrolyte, 2032-type coin cells were assembled in an argon-filled glove box (MBraun Labmaster 130; O_2 and $H_2O<0.1$ ppm) using a hydraulic crimper (MSK-110, MTI corp.). Both the counter electrode (CE) and the reference electrode (RE) were made from a pressed and punched lithium metal disc (MTI corp.) with a diameter of 11 mm and a uniform thickness of 0.45 mm (RE). To separate the working and counter/reference electrodes, vacuum-dried glass-fiber separator (GF/F, Whatman) discs of 18 mm diameter were utilized. A stainless-steel spacer/-current collector was placed on the backside of each counter electrode. The cells were filled with 150 μL 1 M lithium hexafluorophosphate ($LiPF_6$) in an ethylene carbonate (EC) and dimethyl carbonate (DMC) mixture in the ratio EC:DMC (1:1 by volume) as electrolyte (LP30, Sigma Aldrich).

All electrochemical measurements were carried out at a climate chamber (Binder) with a constant temperature of 25 ± 1 °C. Cyclic voltammetry (CV) measurements were performed with a multi-channel potentiostat/galvanostat VMP300 (Bio-Logic Science Instrument), equipped with the EC-Lab software. All CV measurements were carried out with different scan rates of 0.10/0.25/0.50/0.75/ 1.00/2.50/5.00/7.50/10.00 mV s^{-1} in a potential window of 0.01– 3.00 V vs. Li$^+$/Li. Galvanostatic charge-discharge cycling with potential limitation (GCPL) tests in the range of 0.01–3.00 V vs. Li$^+$/ Li with a charge-discharge current of 100 mA g^{-1} were carried out using an Arbin system. The mass of active material was utilized to normalize the specific current and specific capacity calculations. Cells prepared for post-mortem analysis were stopped after 100 cycles in the de*-lithiated state, and the obtained electrode was rinsed with DMC to remove the remaining salt. Rate performance experiments were carried out in the same potential window at different currents to obtain more information about the half-cell rate capacity and higher currents. To get more information about the half-cell rate capability and higher currents, rate performance measurements were conducted by using the same potential window for different currents. The applied specific currents were 0.1 A g^{-1}, 0.2 A g^{-1}, 0.5 A g^{-1}, 1.0 A g^{-1}, 2.0 A g^{-1}, 4.0 A g^{-1}, 8.0 A g^{-1}, and (again) 0.1 A g^{-1}.

Author Contributions

Mana Abdirahman Mohamed: Materials synthesis, measurements, data analysis, writing, plotting, discussion, and manuscript revision. Stefanie Arnold: Electrochemical measurements, writing, plotting, discussion, Raman measurements, and manuscript revision. Oliver Janka: Discussion and manuscript revision. Antje Quade: XPS measurement, plotting, discussion, and manuscript revision. Volker Presser: Supervision, discussion, and manuscript revision. Guido Kickelbick: Conceptualization, supervision, project administration, discussion, and manuscript revision.

Conflict of Interest

The authors declare no conflict of interest.

Data Availability Statement

The data that support the findings of this study are available in the supplementary material of this article.

Keywords: continuous synthesis · electrodes · inorganic-organic hybrid materials · lithium-ion batteries · polyoxometalates

[1] M. Yoshio, H. Wang, K. Fukuda, Y. Hara, Y. Adachi, *J. Electrochem. Soc.* **2000**, *147*, 1245.

[2] A. K. Boehm, S. Husmann, M. Besch, O. Janka, V. Presser, M. Gallei, *ACS Appl. Mater. Interfaces* **2021**, *13*, 61166–61179.

[3] Z. Xiu, D. Kim, M. H. Alfaruqi, J. Song, S. Kim, P. T. Duong, V. Mathew, J. P. Baboo, J. Kim, *J. Alloys Compd.* **2017**, *696*, 143–149.

[4] L. Lu, X. Han, J. Li, J. Hua, M. A. Ouyang, *J. Power Sources* **2013**, *226*, 272–288.

[5] V. Etacheri, R. Marom, R. Elazari, G. Salitra, D. Aurbach, *Energy Environ. Sci.* **2011**, *4*, 3243–3262.

[6] P. Poizot, S. Laruelle, S. Grugeon, L. Dupont, J.-M. Tarascon, *Nature* **2000**, *407*, 496–499.

[7] M. Genovese, K. Lian, *Curr. Opin. Solid State Mater. Sci.* **2015**, *19*, 126–137.

[8] H. Yang, T. Song, L. Liu, A. Devadoss, F. Xia, H. Han, H. Park, W. Sigmund, K. Kwon, U. Paik, *J. Phys. Chem. C* **2013**, *117*, 17376–17381.

[9] F. Li, L. Xu, *Dalton Trans.* **2011**, *40*, 4024–4034.

[10] S. S. Khandolkar, C. Näther, W. Bensch, B. R. Srinivasan, *J. Coord. Chem.* **2016**, *69*, 1166–1178.

[11] M. Y. Zhang, Y. Song, D. Yang, Z. Qin, D. Guo, L. J. Bian, X. G. Sang, X. Sun, X. X. Liu, *Adv. Funct. Mater.* **2021**, *31*, 1–10.

[12] S. S. Khandolkar, P. Raghavaiah, Srinivasan, B. R. Synthesis, *J. Chem. Sci.* **2015**, *127*, 1581–1588.

[13] K. B. Hatzell, M. Beidaghi, J. W. Campos, C. R. Dennison, E. C. Kumbur, Y. A. Gogotsi, *Electrochim. Acta* **2013**, *111*, 888–897.

[14] L. Xu, Y. Sun, B. Han, S. Chang, *J. Electrochem. Soc.* **2019**, *166*, A1363–A1369.

[15] E. Deunf, F. Dolhem, D. Guyomard, J. Simonet, P. Poizot, *Electrochim. Acta* **2018**, *262*, 276–281.

[16] D. Li, Y. Liu, B. Lin, C. Lai, Y. Sun, H. Yang, X. Zhang, *RSC Adv.* **2015**, *5*, 98278–98287.

[17] Q. Huang, T. Wei, M. Zhang, L. Z. Dong, A. M. Zhang, S. L. Li, W. J. Liu, J. Liu, Y. Q. Lan, *J. Mater. Chem. A* **2017**, *5*, 8477–8483.

[18] X. Y. Yang, T. Wei, J. Li, Sen, N. Sheng, P. P. Zhu, J. Q. Sha, T. Wang, Y. Q. Lan, *Inorg. Chem.* **2017**, *56*, 8311–8318.

[19] S. Xia, F. Li, X. Li, F. Cheng, C. Sun, J. J. Liu, H. Guo, *Dalton Trans.* **2018**, *47*, 5166–5170.

[20] W. Cheng, F.-C. Shen, Y.-S. Xue, X. Luo, M. Fang, Y.-Q. Lan, Y. A. Xu, *ACS Appl. Energ. Mater.* **2018**, *1*, 4931–4938.

[21] C. Odenwald, G. Kickelbick, *J. Sol-Gel Sci. Technol.* **2019**, *89*, 343–353.

[22] A. Betke, G. Kickelbick, *Inorganics* **2014**, *2*, 1–15.

[23] B. Krüner, C. Odenwald, A. Tolosa, A. Schreiber, M. Aslan, G. Kickelbick, V. Presser, *Sustain. Energy Fuels* **2017**, *1*, 1588–1600.

[24] B. Krüner, C. Odenwald, N. Jäckel, A. Tolosa, G. Kickelbick, V. Presser, *ACS Appl. Energ. Mater.* **2018**, *1*, 2961–2970.

[25] B. Krüner, C. Odenwald, A. Quade, G. Kickelbick, V. Presser, *Batteries & Supercaps* **2018**, *1*, 135–148.

[26] S. Fleischmann, A. Tolosa, V. Presser, *Chem. Eur. J.* **2018**, *24*, 12143–12153.

[27] C. Ge, P. Jiang, W. Cui, Z. Pu, Z. Xing, A. M. Asiri, A. Y. Obaid, X. Sun, J. Tian, *Electrochim. Acta* **2014**, *134*, 182–186.

[28] F. Cataldo, *Eur. Polym. J.* **1996**, *32*, 43–50.

[29] K. Ohno, M. Okimura, N. Akai, Y. Katsumoto, *Phys. Chem. Chem. Phys.* **2005**, *7*, 3005–3014.

[30] M. Pang, X. Wang, W. Xia, M. Muhler, C. Liang, *Ind. Eng. Chem. Res.* **2013**, *52*, 4564–4571.

[31] Z. Shi, B. Gao, Q. Mo, Z. J. Shao, K. Nie, B. Liu, H. Zhang, Y. Wang, Y. Zhang, Q. Gao, X. Sun, X. M. Cao, P. Hu, Y. Tang, *ChemNanoMat* **2018**, *4*, 194–202.

[32] Q. Gao, C. Zhang, S. Xie, W. Hua, Y. Zhang, N. Ren, H. Xu, Y. Tang, *Chem. Mater.* **2009**, *21*, 5560–5562.

[33] A. Davantès, G. Lefèvre, *J. Phys. Chem. A* **2013**, *117*, 12922–12929.

[34] S. Upreti, A. Ramanan, *Cryst. Growth Des.* **2005**, *5*, 1837–1843.

[35] *Handbook of Chemistry and Physics*, 98th Ed. (Eds.: J. R. Rumble, D. R. Lide, T. J. Bruno), CRC Press: Boca Raton **2017**.

[36] A. Müller, E. Krickemeyer, H. Bögge, M. Schmidtmann, F. Peters, C. Menke, J. Meyer, *Angew. Chem.* **1997**, *109*, 499–502; *Angew. Chem. Int. Ed.* **1997**, *36*, 484–486.

[37] J. Aveston, E. W. Anacker, J. S. Johnson, *Inorg. Chem.* **1964**, *3*, 735–746.

[38] W. F. Chen, C. H. Wang, K. Sasaki, N. Marinkovic, W. Xu, J. T. Muckerman, Y. Zhu, R. R. Adzic, *Energy Environ. Sci.* **2013**, *6*, 943–951.

[39] H. C. Zeng, *J. Cryst. Growth* **1998**, *186*, 393–402.

[40] H. C. Zeng, C. W. Sheu, H. C. Hia, *Chem. Mater.* **1998**, *10*, 974–979.

[41] S. Balakumar, H. C. Zeng, *J. Cryst. Growth* **1999**, *197*, 186–194.

[42] V. V. Atuchin, T. A. Gavrilova, T. I. Grigorieva, N. V. Kuratieva, K. A. Okotrub, N. V. Pervukhina, N. V. Surovtsev, *J. Cryst. Growth* **2011**, *318*, 987–990.

[43] J. S. Chen, Y. L. Cheah, S. Madhavi, X. W. Lou, *J. Phys. Chem. C* **2010**, *114*, 8675–8678.

[44] V. Augustyn, J. Come, M. A. Lowe, J. W. Kim, P. L. Taberna, S. H. Tolbert, H. D. Abruña, P. Simon, B. Dunn, *Nat. Mater.* **2013**, *12*, 518–522.

[45] S. Fleischmann, J. B. Mitchell, R. Wang, C. Zhan, D. E. Jiang, V. Presser, V. Augustyn, *Chem. Rev.* **2020**, *120*, 6738–6782.

[46] S. Ardizzone, G. Fregonara, S. Trasatti, *Electrochim. Acta* **2002**, *35*, 263–267.

[47] W. H. Ryu, D. H. Kim, S. H. Kang, H. S. Kwon, *RSC Adv.* **2013**, *3*, 8527–8534.

[48] J. Tang, C. E. Zavala Lugo, S. F. Acuña Guzmán, G. Daniel, V. G. Kessler, G. A. Seisenbaeva, V. G. Pol, *J. Mater. Chem. A* **2016**, *4*, 18107–18115.

[49] S. Fleischmann, Y. Zhang, X. Wang, P. T. Cummings, J. Wu, P. Simon, Y. Gogotsi, V. Presser, V. Augustyn, *Nat. Energy* **2022**, *7*, 222–228.

[50] H. S. Kim, J. B. Cook, H. Lin, J. S. Ko, S. H. Tolbert, V. Ozolins, B. Dunn, *Nat. Mater.* **2017**, *16*, 454–462.

[51] D. Han, S. Hwang, S. M. Bak, K. W. Nam, *Electrochim. Acta* **2021**, *388*, 1–10.

[52] X. Yang, Q. Li, H. Wang, J. Feng, M. Zhang, R. Yuan, Y. Chai, *Chem. Eng. J.* **2018**, *337*, 74–81.

[53] H. Xin, Y. Hai, D. Li, Z. Qiu, Y. Lin, B. Yang, H. Fan, C. Zhu, *Appl. Surf. Sci.* **2018**, *441*, 69–76.

[54] W. Chen, H. Zhang, Y. Wang, Z. Ma, Z. Li, *Electrochim. Acta* **2014**, *144*, 369–375.

[55] J. Han, P. Liu, Y. Ito, X. Guo, A. Hirata, T. Fujita, M. Chen, *Nano Energy* **2018**, *45*, 273–279.

[56] E. Larson, L. Williams, C. Jin, X. Chen, J. DiCesare, O. Shepperd, S. Xu, J. Wu, *J. Mater. Res.* **2021**, 1–12.

[57] N. Naresh, P. Jena, N. Satyanarayana, *J. Alloys Compd.* **2019**, *810*, 1–8.

[58] S. Gao, Y. Tang, H. Zhao, L. Liu, Y. Gu, R. Sheng, *Int. J. Energy Res.* **2021**, *45*, 6418–6425.

[59] U. Kolitsch, *Zeitschrift fuer Krist.* **2001**, *216*, 449–454.

[60] S. M. Sayyah, S. S. Abd El-Rehim, M. M. El-Deeb, S. M. Kamal, R. E. Azooz, *J. Appl. Polym. Sci.* **2010**, *117*, 943–952.

[61] G. Ciric-Marjanovic, B. Marjanović, P. Bober, Z. Rozlívková, J. Stejskal, M. Trchová, J. Prokeš, *J. Polym. Sci. Part A* **2011**, *49*, 3387–3403.

[62] E. Payen, J. Grimblot, S. Kasztelan, *J. Phys. Chem.* **1987**, *91*, 6642–6648.

ChemSusChem

Research Article
doi.org/10.1002/cssc.202202213

Chemistry Europe
European Chemical
Societies Publishing

[63] L. Liu, W. Zhang, P. Guo, K. Wang, J. Wang, H. Qian, I. Kurash, C. H. Wang, Y. W. Yang, F. Xu, *Phys. Chem. Chem. Phys.* **2015**, *17*, 3463–3469.

[64] S. Ikari, Y. Sasaki, T. Ito, *Inorg. Chem.* **1989**, *28*, 447–451.

[65] X. Liu, Y. Lyu, Z. Zhang, H. Li, Y. S. Hu, Z. Wang, Y. Zhao, Q. Kuang, Y. Dong, Z. Liang, Q. Fan, L. Chen, *Nanoscale* **2014**, *6*, 13660–13667.

[66] Bruker AXS, Karlsruhe G 2014 Topas 5.1. General Profile and Structure Analysis Software for Powder Diffraction Data.

[67] Sheldrick, G. M. SHELXT – Integrated Space-Group and Crystal-Structure Determination. *Acta Crystallogr. Sect. A Found. Crystallogr.* **2015**, *A71*, 3–8.

[68] Sheldrick, G. M. Crystal Structure Refinement with SHELXL. *Acta Crystallogr. Sect. C Struct. Chem.* **2015**, *C71*, 3–8.

[69] Hübschle, C. B.; Sheldrick, G. M.; Dittrich, B. ShelXle: A Qt Graphical User Interface for SHELXL. *J. Appl. Crystallogr.* **2011**, *44*, 1281–1284.